Interfacial Mechanical Properties of n-Alkylsilane Monolayers on Silicon Substrates

Brian G. Bush, Frank W. Del Rio, Cherno Jaye, Daniel A. Fischer, and Robert F. Cook

Abstract—The interfacial properties of n-alkylsilane monolayers on silicon were investigated by normal force spectroscopy, lateral force measurements, and near-edge X-ray absorption fine structure (NEXAFS) spectroscopy. Monolayers of $(CH_3(CH_2)_{n-1}SiCl_3)$ with chain lengths $n = 5, 8, 12$, and 18 were prepared and NEXAFS spectra were used to compute the dichroic ratio, R_I. As n decreased from 18 to 5, the film structures change from ordered ($R_I = 0.41$) to disordered ($R_I = 0.12$) states. Normal force spectroscopy data were analyzed with a modified elastic adhesive contact model to extract Young's modulus, E_{film}, and the work of adhesion, w, of the film; E_{film} decreased from 1.2 to 0.67 GPa, and w increased from 48.6 to 60.1 mJ $\cdot$ m^{-2} as n decreased from 18 to 5. Lateral force measurements quantified the reduction in friction via an interfacial shear strength, τ, and a lateral deformation analog, η. Monolayer adsorption reduced τ from 3500 MPa for SiO$_2$ to less than 50 MPa for $n = 12$ and 18 alkylsilanes and was dependent on contact pressure. Conversely, η was pressure invariant, with values of ≈ 3500 MPa for $n = 5$ and 8 and ≈ 1000 MPa for $n = 12$ and 18. [2012-0165]

Index Terms—Friction, interface phenomena, microelectromechanical devices, reliability, silicon, surface treatment.

I. INTRODUCTION

SINCE the early 1980s, designers and manufacturers of microelectromechanical systems (MEMS) have developed a wide variety of novel devices capable of many sensing and actuating functions, including freestanding cantilever beams [1], pressure transducers [2], comb-drive resonators [3], inertial navigation systems including accelerometers and gyroscopes, and high resolution digital mirror displays [4], [5]. Despite the progress of the MEMS industry, however, issues related to device reliability remain a major factor inhibiting further advancement of MEMS commercialization. Reliability issues arise because MEMS devices have small lateral dimensions and, therefore, large surface-area-to-volume ratios, thus enabling surface interactions, such as adhesion and friction, to overwhelm device restoring forces and cause failure [6]. To date, few MEMS products have been developed and commercialized that contain contacting or sliding surfaces, and even

the most notable, the digital mirror array, requires special hermetic encapsulation and complex surface lubricants to function reliably [5]. As a result, MEMS designers remain unable to exploit MEMS technology to its full potential and have yet to realize the tremendous promise of elaborate and quality-of-life enhancing applications such as biomedical implantable actuators for sensing blood chemistry or for insulin regulation, drug delivery systems, MEMS-based energy harvesting devices, microengines for lightweight energy production and storage, and ultralow power consumption electrical and mechanical switches [7].

The primary factor inhibiting device reliability is failure due to adhesion and friction effects at interfacial contacts of device components. For example, MEMS comb-drive resonators and pop-up mirrors have been shown to fail readily due to capillary meniscus condensation and subsequent capillary adhesion [8], while MEMS gears may fail due to friction between the gear and hub [8] or by adhesion between the gear and substrate [9]. At present, MEMS designers are forced to circumvent failure due to large adhesion and friction forces by designing MEMS that minimize contact or avoid it altogether as in the comb-drive resonators and accelerometers mentioned earlier. The necessity of designing and incorporating special bumpers and contact points to minimize interfacial contact area between components increases device complexity and adds additional processing steps during fabrication. Similarly, failure due to adhesion and friction can be circumvented by overpowering the contact through high driving and restoring forces or packaging strategies [10], but the necessity of having large driving and restoring forces will also limit the minimum dimensions attainable for devices as surface interactions become relatively stronger at the nanoscale. These strategies make the design of MEMS more complex and can reduce their overall efficiency in terms of sensitivity, performance, power consumption, and cost.

Another commonly used method to combat failure due to adhesion and friction in MEMS is to employ self-assembled monolayers (SAMs) to chemically modify the component surfaces, thereby altering the relevant adhesion and friction interactions. SAMs exist for a wide variety of surfaces, including alkanethiols [$CH_3(CH_2)_{n-1}SH$, where n is the number of carbons in the SAM chain] for metal surfaces such as Au, n-alkanoic fatty acids ($C_nH_{2n+1}COOH$) for metal oxides such as Al$_2$O$_3$, and n-alkylsilane ($CH_3(CH_2)_{n-1}SiCl_3$) SAMs for Si and its oxide [11]. Perhaps the most widely studied class of SAMs is that of alkanethiols adsorbed onto Au due to the relative ease of the adsorption process; the Au–thiol system

has enabled sensitive measurements of the interfacial [12], elastic [13]–[15], and charge transport [15], [16] properties of SAMs via scanning probe microscopy, surface spectroscopy, and other means. Although these measurements are important from a fundamental standpoint, the Au–thiol system does not accurately reflect the types of interactions encountered in silicon-based MEMS coated with their SAM counterpart, i.e., alkylsilane monolayers. As with other SAMs, alkylsilane monolayers have shown great promise in reducing adhesion and friction and therefore improving performance and reliability in simple MEMS devices [17], [18]. More recently, alkylsilane and fluorinated alkylsilane SAMs were used to enhance the reliability of the "nanotractor," a complex polycrystalline silicon MEMS device used to assess friction and wear [19]. However, unlike the Au–thiol system, the preparation of alkylsilane SAMs on silicon is not straightforward, and as a result, fundamental studies on their adhesion and friction properties are not as mature.

Early studies on the adhesion and friction properties of alkylsilane SAMs were performed on mica substrates [20]–[22]. Mica provides an attractive substrate for such fundamental studies, as siloxane bonds do not form between the molecules and substrate, thereby allowing a direct assessment of molecule–molecule interactions [20]. However, as with the Au–thiol studies, this poorly approximates the type of interactions encountered in real silicon-based MEMS devices. Later work with alkylsilanes used single-crystal silicon as the substrate material and showed significant decreases in both adhesion and friction, with the reductions in each dependent on measurement solution pH [23] and relative humidity [24] and chain length and phase state [25]. More recently, Flater *et al.* [26] used atomic force microscopy (AFM) to show that adhesion and friction behavior is also dependent on which surface is coated with the SAM—the AFM probe tip or the silicon substrate. For a SAM-coated tip in contact with a silicon substrate, the friction varied sublinearly with applied load, in agreement with continuum contact mechanics models. However, for a bare AFM tip in contact with a SAM-coated silicon substrate, the friction varied superlinearly with applied load. In this configuration, friction was mostly attributed to molecular deformation and localized chain rearrangement at the leading edge of the AFM probe tip rather than purely interfacial interactions [26], [27]. That is, the friction was not due to adhesion hysteresis alone [24], [28]. Due to the complex nature of the SAM–substrate mechanical properties, however, none of these studies were able to accurately account for the substrate and thus extract fundamental properties of the alkylsilane monolayer, such as the interfacial shear strength, τ, and its lateral deformation analog, η.

In this paper, the elastic and interfacial properties of methyl-terminated alkylsilane SAMs of varying chain length and molecular phase are investigated by normal and lateral force AFM. Normal force AFM data are analyzed with the Derjaguin–Muller–Toporov (DMT) contact model [29], [30], modified by a first-order elastic perturbation method to include substrate effects, to determine the elastic modulus of the monolayer as a function of n [31]. Using the monolayer mechanical properties and a diamagnetic lateral force calibration technique

[32] to determine the torsional spring constant of the AFM probe, the lateral force AFM data are used to calculate upper bounds for both τ and η as a function of n. In addition, the mechanical properties are correlated with molecular structure as given by near-edge X-ray absorption fine structure (NEXAFS) spectroscopy. Specifically, carbon K-edge spectra are used to compute the dichroic ratio for each monolayer, which provides a quantitative measure of molecular structure. Taken together, the AFM and NEXAFS results provide structure–property relationships for alkylsilane SAMs on silicon substrates and a general methodology for the optimization of SAMs for MEMS devices with both contacting and sliding surfaces.

II. EXPERIMENTAL METHODS

A. Sample Preparation

Alkylsilanes of $n = 8$ and $n = 18$, as well as anhydrous hexadecane and carbon tetrachloride, were purchased from Sigma Aldrich (Milwaukee, WI); the latter two were used as received. Alkylsilanes of $n = 5$ and $n = 12$ were obtained from Santa Cruz Biotechnology (Santa Cruz, CA) and Alfa Aesar (Ward Hill, MA), respectively. Silicon (100) wafers cut to a size of 8 mm × 8 mm were used as the substrates for all n. All substrates were sonicated in isopropanol for 5 min, rinsed with 2:1 H_2SO_4 : H_2O_2 piranha solution for 10 min, etched briefly in 48% HF solution to remove any native oxide, and then reimmersed in a 2:1 piranha solution for 10 min prior to silanization. The second piranha exposure aids in the formation of a thin oxide layer on the silicon surface that is helpful for ensuring complete silanization [33]. Following the cleaning step, the Si (100) substrates were immersed in 1-mM alkylsilane solutions of 3:2 hexadecane:carbon tetrachloride for 60 min inside a low-humidity glove box (Electro-Tech Systems, Series 5503, Glenside, PA) with a relative humidity of approximately 5%. The low relative humidity provides for enough water to be adsorbed into the solvent to facilitate silanization without promoting bulk agglomeration of the precursor in solution [34]. Alkylsilane monolayers of $n = 5$ and 8 were prepared at room temperature ($T = 20$ °C), while monolayers of $n = 12$ and 18 were prepared at two variant temperatures, $T = 40$ °C for liquid-expanded phase monolayers and $T = 0$ °C for their condensed-phase counterparts [35]. In addition, the low-temperature samples were adsorbed via two 30-min solution immersions rather than a single 60-min immersion; refreshing the solution midway was found to be necessary at low temperatures, as the solutions tended to condense water from the atmosphere rather quickly, leading to bulk agglomeration. Hereafter, the $n = 12$ and 18 liquid-expanded phase monolayers will be referred to as 12e and 18e, respectively, whereas the low temperature adsorbed phases will be denoted simply as $n = 12$ and 18.

B. NEXAFS Spectroscopy

NEXAFS measurements were carried out at the National Institute of Standards and Technology (NIST) U7A beamline of the National Synchrotron Light Source. Partial

electron yield (PEY) spectra at the carbon K-edge, 270 to 340 eV (1 eV $= 1.6 \times 10^{-19}$ J), were obtained with a channeltron retarding voltage of -150 V to enhance surface sensitivity and Auger yield. Drain currents of a carbon mesh and a clean gold mesh, both located in the path of the incident linearly polarized photon beam, were measured to aid in energy calibration and normalization of the PEY signal, respectively. NEXAFS spectra were taken at angles θ ranging from $20°$ to $90°$, measured between the sample surface and the photon beam.

C. Normal Force Spectroscopy

Normal force spectroscopy was carried out in a Bruker Nanoscope V scanning probe microscope (Santa Barbara, CA). Si cantilever probes coated with 60 nm of Co followed by 20 nm of Cr (NSC19/Co-Cr) from Mikromasch (San Jose, CA) were used for the measurements. The cantilever spring constant in the normal direction, k_N, was determined by the thermal fluctuation method [36] and found to be 1.51 N $\cdot$ m^{-1} ± 0.03 N $\cdot$ m^{-1}, where the uncertainty is calculated as two standard deviations of the mean of ten measurements. Normal force data were captured with a maximum normal load of 15 nN and fit to the DMT contact model modified by a first-order elastic perturbation method to extract the film modulus and work of adhesion. Finally, the probe tip radius R was determined by imaging Si nanowires in noncontact mode and using the blind reconstruction method [37]; with this method, R was found to be about 38 nm $\pm$ 5 nm.

D. Lateral Force Measurements

Lateral force measurements were also carried out in the same microscope with the same cantilever probes as the normal force measurements. The experiments were conducted with a lateral tip velocity of 8 μm $\cdot$ s^{-1} and normal forces ranging from 2.5 to 100 nN. The calibration of the cantilever torsional response was performed using a diamagnetic lateral force calibration (D-LFC) technique. D-LFC uses four NdFeB magnets and a diamagnetic pyrolytic graphite shuttle to quantify the lateral force calibration factor with a relative precision of 0.1% [32]. In the D-LFC approach, the cantilever is held stationary, with its tip in contact with the graphite shuttle, which is levitating above the four magnets. When the four magnets are displaced laterally by the piezoelectric displacement actuator of the AFM, the shuttle attempts to return to its equilibrium position above the magnets, thereby twisting the cantilever and changing the differential voltage output of the AFM split photodiode sensor. To relate the applied lateral force of the cantilever to the voltage output on the photodiode, it is first necessary to calculate the spring constant of the D-LFC setup by measuring the natural vibration frequencies of the system (i.e., without the tip in contact with the graphite shuttle). For the D-LFC assembly, the spring constant was found to be 0.043 N $\cdot$ m^{-1} ± 0.004 N $\cdot$ m^{-1}, where the uncertainty was calculated as two standard deviations of the mean. Once the D-LFC spring constant is known, the cantilever lateral force calibration constant can be determined. For the AFM cantilevers, the force calibration

TABLE I
WATER CONTACT ANGLE θ_{H2O} AND MONOLAYER THICKNESS t AS MEASURED BY GONIOMETRY AND SPECTROSCOPIC ELLIPSOMETRY FOR $n = 5, 8, 12e, 12, 18e,$ AND 18. UNCERTAINTY VALUES REPRESENT TWO STANDARD DEVIATIONS OF THE MEAN

n	θ_{H2O} (°)	t (nm)
5	97.9 ± 2.6	0.80 ± 0.17
8	103.0 ± 3.4	0.97 ± 0.11
12e	106.8 ± 2.6	1.21 ± 0.06
12	108.8 ± 1.6	1.44 ± 0.04
18e	109.4 ± 2.0	2.34 ± 0.09
18	109.9 ± 2.0	2.32 ± 0.07

constant was determined to be 43.9 nN $\cdot$ V^{-1} ± 0.5 nN $\cdot$ V^{-1}, where the uncertainty represents two standard deviations from the mean of eight calibration measurements.

III. RESULTS

A. Molecular Orientation, Relative Order, and Surface Coverage

After silanization, samples were characterized by water contact angle goniometry and spectroscopic ellipsometry to ensure complete monolayer formation, the results of which are summarized in Table I. The static water contact angles decreased from $109.9°$ to $98°$ as the chain length decreased from 18 to 5. These values are consistent with previous studies for hydrocarbon monolayers [15], [38] and indicate that, as n decreases, the monolayer exposes additional CH$_2$ groups and thus becomes more hydrophilic. Assuming an index of refraction of $n_{\mathrm{f}} = 1.45$ for all n, the spectroscopic ellipsometry measurements showed that the film thickness t decreased from 2.32 to 0.80 nm as n decreased from 18 to 5. For $n = 18$, t was close to the theoretical molecular chain length [39], which suggests that monolayers formed from $n = 18$ molecules exhibit a densely packed nearly vertical chain orientation [40].

NEXAFS PEY spectra at the carbon K-edge for $n = 5$, 8, 12e, 12, 18e, and 18 at angles $\theta = 20°$, $44°$, and $70°$ are shown in Fig. 1(a) and clearly exhibit relevant hydrocarbon resonances: the C–H σ^* resonance at 288.6 eV and the C–C σ^* resonance at 293.6 eV [41]. The spectra for $n = 5$ and 8 are nearly identical for all θ, suggesting that the short-chain monolayers exhibit relatively high molecular disorder and consist of loosely packed liquidlike monolayers. Longer chain lengths (e.g., $n = 12$ and 18) exhibit increasing C–H σ^* resonance and decreasing C–C σ^* resonance as θ increases, suggesting that monolayers formed from longer hydrocarbons are relatively more ordered with near vertically aligned carbon backbones. The normalized peak intensities were quantified by subtracting an integrated Lorentzian continuum step from the raw spectra, fitting Gaussian peaks to the resultant spectra, and extracting the peak height. The Lorentzian continuum step function is given as [41]

$$I_{\mathrm{step}}^{\mathrm{exp}} = H \left[\frac{1}{2} - \frac{1}{\pi} \arctan \left(\frac{E - P}{\frac{\Gamma_{\mathrm{L}}}{2}} \right) \right] \quad (1)$$
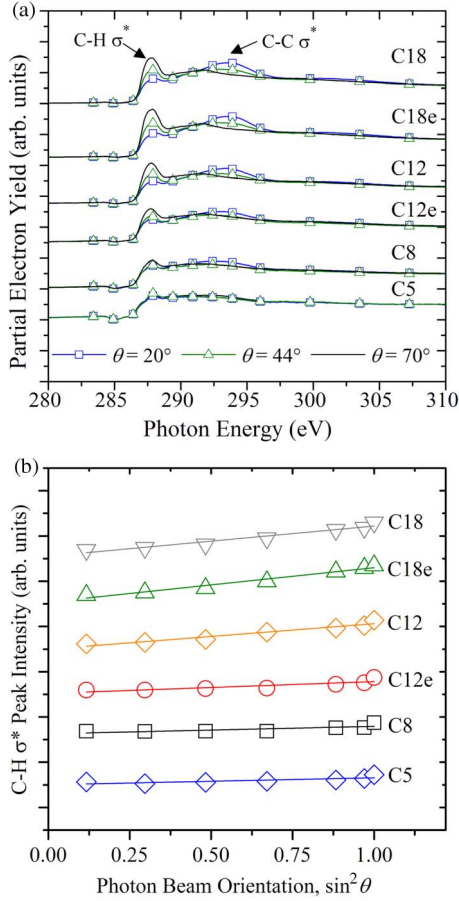
Fig. 1. (a) NEXAFS carbon K-edge PEY spectra for $n = 5, 8, 12e, 12, 18e$, and 18. (b) NEXAFS C–H σ^* peak intensities as a function of $\sin^2 \theta$ for $n = 5$, 8, 12e, 12, 18e, and 18. Intensity values have been offset for clarity.

for $E \leq P + \Gamma_{\mathrm{L}}$ and

$$I_{\mathrm{step}}^{\mathrm{exp}} = H \left[\frac{1}{2} - \frac{1}{\pi} \arctan \left(\frac{E - P}{\frac{\Gamma_{\mathrm{L}}}{2}} \right) \right] \cdot \exp\left[-d(E - P - \Gamma_{\mathrm{L}}) \right] \tag{2}$$

for $E > P + \Gamma_{\mathrm{L}}$, where E is the electron energy, H is the step height, P is the step inflection point, Γ_{L} is the step width, and d is the decay coefficient. The model parameter values are somewhat arbitrary [42], [43] and were chosen such that the step edge accurately reflected the decay observed in all spectra. The step function parameters chosen for this analysis were $H = 1.2$, $P = 290$ eV, $\Gamma_{\mathrm{L}} = 1$ eV, and $d = 0.008$ (eV)$^{-1}$.

The resulting C–H σ^* peak intensities are plotted as a function of $\sin^2 \theta$ in Fig. 1(b). Peak intensity variation with θ is correlated with relative molecular orientation through the dichroic ratio, R_{I}, where $R_{\mathrm{I}} = (I_{90°} - I_{0°})/(I_{90°} + I_{0°})$. In this expression, $I_{90°}$ is the fitted peak intensity for the sample surface perpendicular to the incident beam and $I_{0°}$ is the ($\sin^2 \theta$ linearly) extrapolated peak intensity for a sample surface parallel to the incident beam [41]. R_{I} can vary from -1 to $+0.75$, with a more positive value for the C–H σ^* peak corresponding to greater surface normality and molecular order ($R_{\mathrm{I}} = 0$ may represent a random distribution of chain orientations). Table II summarizes the C–H σ^* dichroic ratios for all monolayer chain lengths and adsorption phases investigated; for $n = 18$ and 18e,

TABLE II
DICHROIC RATIO R_{I}, WORK OF ADHESION w, AND YOUNG'S MODULUS E_{film} FOR $n = 5, 8, 12e, 12, 18e$, AND 18. UNCERTAINTY VALUES REPRESENT A 95% CONFIDENCE LEVEL IN THE FIT[a] OR TWO STANDARD DEVIATIONS OF THE MEAN[b]

n	R_{I} C–H $\sigma^{*\mathrm{a}}$	w (mJ m^{-2})[b]	E_{film} (GPa)[b]
5	0.13 ± 0.06	60.1 ± 3.8	0.67 ± 0.13
8	0.12 ± 0.06	52.5 ± 3.4	0.93 ± 0.75
12e	0.20 ± 0.07	54.4 ± 3.7	1.01 ± 0.58
12	0.36 ± 0.06	49.2 ± 3.3	1.03 ± 0.65
18e	0.41 ± 0.05	50.5 ± 4.7	1.20 ± 0.37
18	0.38 ± 0.06	48.6 ± 4.2	1.13 ± 0.39

$R_{\mathrm{I}} \approx 0.4$, which is indicative of a highly ordered monolayer consisting of a densely packed film with vertically oriented alkyl chains. As n decreased from 18 to 5, R_{I} also decreased from 0.41 to 0.12, indicating that alkylsilane films become relatively more disordered or liquidlike as the chain length decreases. Moreover, it might be anticipated that the liquid-expanded phase monolayers for $n = 12$ and 18 would exhibit a measurable increase in molecular disorder. For $n = 12$, the liquid-expanded phase monolayers indeed resulted in smaller values for R_{I} than their condensed-phase counterparts, providing evidence in support of this hypothesis. However, this was not the case for all n, as the dichroic ratios for $n = 18$ and 18e were the same within experimental uncertainty.

B. Elastic and Interfacial Properties

AFM was used to conduct normal force spectroscopy on each alkylsilane monolayer and a bare SiO^2 substrate. Normal force (F_{N})–displacement (d) curves were converted to normal force–indentation depth (δ) data by subtracting the deflection of the cantilever, $F_{\mathrm{N}}/k_{\mathrm{N}}$, from each displacement value. AFM $F_{\mathrm{N}} - \delta$ data (in the unloading direction) for all n are shown in Fig. 2. Young's modulus, E_{film}, and work of adhesion, w, of each film were extracted from the $F_{\mathrm{N}} - \delta$ data with the DMT contact model, an elastic contact theory that accounts for adhesive forces in the response of a tip of radius R interacting with a flat surface [29], [30]

$$F_N = \frac{4}{3} E^* R^{\frac{1}{2}} \delta^{\frac{3}{2}} - 2\pi R w \tag{3}$$

where E^* is the effective modulus of the contact. An analytical model for the effective modulus of a film–substrate system was used that accounts for both the modulus and Poisson's ratio of the substrate (E_{sub} and ν_{sub}) and those of the film (E_{film} and ν_{film}) and gives an accurate description of the effective elastic compliance of the film–substrate system. Here, E^* is given by [44]

$$\frac{1}{E^*} = \frac{1}{2} \left[1 - \nu_{\mathrm{sub}} + (\nu_{\mathrm{sub}} - \nu_{\mathrm{film}}) I_1 \right]$$
$$\cdot \left[\frac{2(1 + \nu_{\mathrm{sub}})}{E_{\mathrm{sub}}} (1 - I_0) + \frac{2(1 + \nu_{\mathrm{film}})}{E_{\mathrm{film}}} I_0 \right] \tag{4}$$
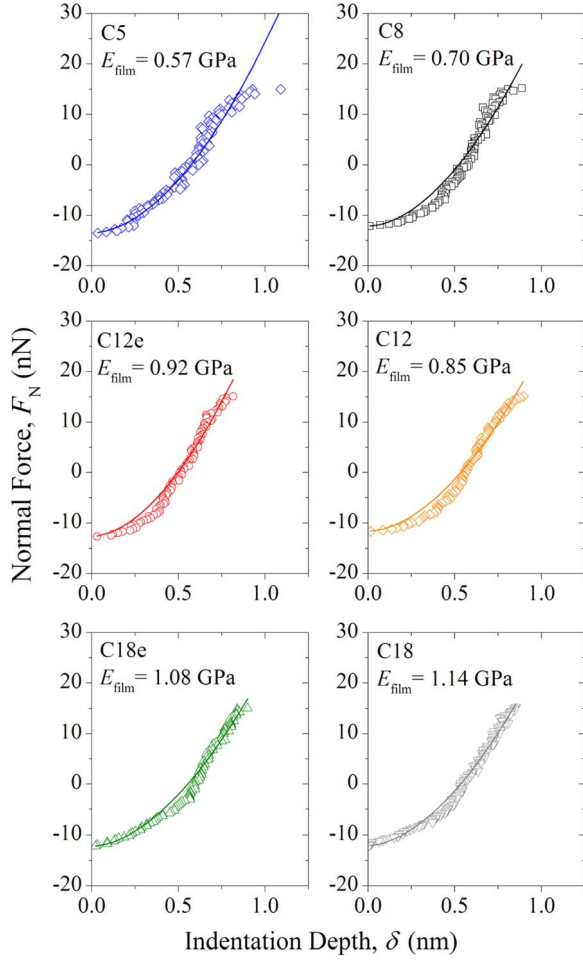
Fig. 2. $F_N - \delta$ (symbols) experimental data and (solid lines) curve fits for $n = 5, 8, 12e, 12, 18e,$ and 18. The curve fits are based on the extended DMT contact model, using w and E_{film} as the fitting parameters (E_{film} values shown here are not the average values but the values for the specific experimental data shown). R^2 values for the fits to the data were typically greater than 0.90.

where I_0 and I_1 are weighting functions that account for differences in film and substrate shear modulus and Poisson's ratio, respectively. I_0 and I_1 are defined as [44]

$$I_0(\xi) = \frac{2}{\pi} \arctan \xi + \frac{1}{2\pi(1 - \nu_{\text{sub}})}$$
$$\cdot \left[(1 - 2\nu_{\text{sub}})\xi \ln \frac{1 + \xi^2}{\xi^2} - \frac{\xi}{1 + \xi^2} \right] \quad (5)$$

and

$$I_1(\xi) = \frac{2}{\pi} \arctan \xi + \frac{\xi}{\pi} \ln \frac{1 + \xi^2}{\xi^2} \quad (6)$$

where $\xi = t/a$ is the normalized film thickness, defined as the ratio of the film thickness t to the contact radius $a = (R\delta)^{1/2}$. $E_{\text{sub}} = 165$ GPa and $\nu_{\text{sub}} = 0.22$ were used for the silicon (100) substrate [45], and $\nu_{\text{film}} = 0.44$ was used for the monolayer film [46]. To find w, (3) was solved at $\delta = 0$, which results in $w = -F_{\text{po}}/2\pi R$, where F_{po} is the pull-off force from each $F_N - \delta$ data set. Similarly, to find E_{film}, the DMT model was fit to the full $F_N - \delta$ traces as shown in Fig. 2, using (4) for the effective modulus E^* and E_{film} as the fitting parameter. The
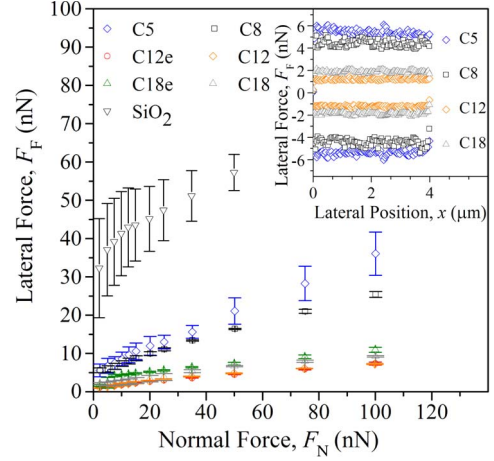

Fig. 3. Lateral friction force F_F as a function of applied normal force F_N for $n = 5, 8, 12e, 12, 18e,$ and 18 and a bare SiO_2 substrate. (Inset) Corresponding friction loops for $n = 5, 8, 12,$ and 18. Error bars represent two standard deviations from mean.

results for w and E_{film} are given in Table II. As n decreased from 18 to 5, w increased from 48.6 to 60.1 mJ·m^{-2}, and E_{film} decreased from 1.2 to 0.67 GPa; these broad trends can be explained in terms of a decrease in the stabilization forces between alkyl chains, which thus also reduces the film's resistance to elastic deformation (i.e., decreases E_{film}) and exposes the tip to additional functional groups in the film or to the substrate (i.e., increases w). Moreover, it was found that liquid-expanded phase monolayers exhibited larger w than liquid-condensed phase monolayers, despite having nearly identical E_{film}.

AFM was also used to conduct lateral force measurements for each alkylsilane monolayer and a bare SiO_2 substrate. The differential voltage output of the split photodiode was converted to a lateral force F_F using the D-LFC calibration technique described previously, the results of which are shown in Fig. 3 as a function of F_N for $n = 5, 8, 12e, 12, 18e,$ and 18 and a bare SiO_2 substrate. Corresponding friction loops in the trace (upper) and retrace (lower) directions for $n = 5, 8, 12,$ and 18 at $F_N = 15$ nN are also included as an inset. As expected, the bare SiO_2 substrate exhibited the greatest lateral force and varied sublinearly with applied load, a phenomenon that is well described by continuum linear elasticity. Overall, F_F was substantially reduced for the alkylsilane films, with F_F increasing toward that of bare SiO_2 as n decreased from 18 to 5. Two notable exceptions were $n = 12$ and 12e, which exhibited smaller values for F_F than $n = 18$ and 18e, respectively. Additionally, F_F varied almost linearly with F_N for all n.

IV. DISCUSSION

NEXAFS carbon K-edge spectra were used to compute the dichroic ratio R_I for each film, which provided a quantitative measure of the molecular structure as a function of chain length and deposition temperature. As shown in Table II, R_I decreased as n decreased, which points to a structural dependence on n. Furthermore, from the R_I results, it is clear that there is a change in phase from crystalline to amorphous in the region $8 < n < 12$. The trends here are consistent with external reflection infrared spectroscopy experiments, which suggests

that long-chain alkylsilanes ($n \geq 13$) form densely packed crystallinelike monolayers, while short-chain alkylsilanes ($n = 10$) exhibit an increased amount of conformational disorder as indicated by frequency shifts and band broadenings of the CH stretching absorptions [47]. Sambasivan *et al.* [48] reported a similar crystalline to amorphous transition chain length ($5 < n < 10$) for alkylsilanes on silicon but noted smaller values and different trends for R_I. For example, $n = 12$ (not $n = 18$) was found to be the most crystalline monolayer in their study, with a dichroic ratio of only $R_I = 0.28$. For smaller and larger values of n, R_I decreased to ≈ 0. Genzer *et al.* [49] showed that such variations in R_I for similar monolayers can be the result of differences in molecular grafting density; as grafting density decreases, average tilt angle increases, which results in smaller R_I values. Thus, the smaller values for R_I could be due to smaller grafting densities (i.e., incomplete monolayer formation), which would also explain their modest water contact angles for all n (e.g., 95.4° for $n = 18$).

AFM normal force spectroscopy was used to determine w and E_{film} for each film, which provided insight into the adhesive and elastic properties in terms of chain length and deposition temperature. For $n = 18$, $w = 48.6 \, \text{mJ} \cdot \text{m}^{-2}$, which is in good agreement with the results from bulk contact angle studies of similar long-chain *n*-alkyl monolayers, $46 \, \text{mJ} \cdot \text{m}^{-2}$ [50]. Also, the value is consistent with results from the Lifshitz theory, which indicates that the adhesion can be attributed predominately to van der Waals forces [51], [52]. However, as n decreased, w increased. Berger *et al.* [53] noted a similar trend for phase-separated lipid monolayers and attributed the change in w to differences in molecular orientation and order. In the liquid-condensed domains, the molecules were densely packed, and the probe tip interacted only with the CH_3 end groups, whereas in the liquid-expanded domains, the films were liquidlike, and the adhesion was mainly due to CH_2 groups along the hydrocarbon chain. Given that $\gamma_{\text{CH2}} = 31 \, \text{mJ} \cdot \text{m}^{-2}$ and $\gamma_{\text{CH3}} = 23 \, \text{mJ} \cdot \text{m}^{-2}$, it was shown that $w_{\text{CH2}}/w_{\text{CH3}} = (\gamma_{\text{CH2}}/\gamma_{\text{CH3}})^{1/2} = 1.2$, where γ_a and w_a are the surface energy and the work of adhesion for molecule a, respectively. From Table II, $w_{\text{C5}}/w_{\text{C18}} = 1.2$, which similarly suggests that the probe tip interacts primarily with CH_3 groups in the case of $n = 18$ and with CH_2 groups in the case of $n = 5$ for alkylsilane monolayers on silicon.

Interestingly, the values for w were much smaller than those for alkanethiol monolayers on gold measured through similar means [31]. This behavior can be explained as a consequence of two factors. First, greater works of adhesion are anticipated for alkanethiol monolayers on gold as compared to alkylsilane monolayers on SiO_2 because gold exhibits a Hamaker constant nearly twice that of SiO_2 [54]. Second, because alkylsilanes exhibit a smaller average tilt angle (i.e., more vertical chain orientation) than alkanethiols, the probe tip interacts with more CH_3 terminal groups, resulting in smaller values for w as demonstrated with the CH_3/CH_2 surface energy argument mentioned earlier. Additionally, the $w_{\text{C5}}/w_{\text{C18}}$ ratio for alkylsilanes on silicon, $w_{\text{C5}}/w_{\text{C18}} = 1.2$, was much smaller than that for alkanethiols on gold, $w_{\text{C5}}/w_{\text{C18}} = 2.0$. For short-chain alkanethiols on gold ($n < 8$), a lack of cohesive energy leads to the thermal desorption of low surface energy alkyl

chains [55] and subsequent absorption of high surface energy adventitious hydrocarbons, as demonstrated by an increase in the $C = C \, \pi^*$ resonance peak from NEXAFS measurements [31]. Thus, the increase in w as n decreased was not only due to an increase in the CH_2 interactions but also from additional high surface energy contributions at the interface (i.e., the adventitious hydrocarbons and the gold substrate). For the short-chain alkylsilanes on silicon, no such desorption–absorption process takes place, as evident from the lack of a $C = C \, \pi^*$ peak in Fig. 1(a). As a result, the changes in w were simply governed by the CH_3/CH_2 ratio.

The variation of E_{film} with n can be explained in terms of changes in the attractive van der Waals interactions between alkyl chains with n [21]. As n increases for densely packed chains, the van der Waals stabilization force provided by additional CH_2 groups decreases and eventually saturates at $n \approx 10$. Consequently, E_{film} should be almost invariant for large n and then decrease with decreasing n for small n, both of which were observed experimentally (see Table II). The variation mechanism is consistent with the NEXAFS data in Fig. 1(a), which also pointed to an increase in molecular tilt relative to the normal followed by a change in phase for decreasing n. Therefore, the reported uncertainty for E_{film} consists of both experimental measurement uncertainty and physical variability in the properties of the film. As might have been anticipated, the relative uncertainty of films in the transition region ($n \approx 10$) is greatest, reflecting this variability.

Overall, the E_{film} results in Table II are in good agreement with those for low-density and high-density polyethylene [56]. Similarly, the results are consistent with interfacial force microscope experiments on long-chain alkylsilane monolayers on SiO_2, which resulted in an initial tangent modulus of 1.5 GPa [46]. In contrast, however, the values are at least 20% greater than those extracted from similar studies on alkanethiols on gold and alkylphosphonates on indium tin oxide [47]. The larger elastic moduli for alkylsilanes on silicon relative to those for other methyl-terminated alkyl SAMs indicate that the siloxane cross-linking network at the base of the alkylsilane monolayer may play an important role in its enhanced resistance to elastic deformation; an analogous increase in mechanical strength was observed during a comparative study of analogous monolayers [20]. Such comparisons are only possible when substrate properties are taken into account, thus generating film properties that are not artificially inflated [58].

Using the results in Table II, the measured tip radius R, and a value for a characteristic length scale z_0, it is possible to calculate the Tabor parameter $\mu = \left(Rw^2/E^{*2}z_0^3\right)^{1/3}$, a dimensionless quantity used to test the applicability of the various contact models [59]. For example, the DMT contact model [29], [30] used earlier is suitable for stiff contacts with small long-range attractive forces ($\mu < 1$), while the Johnson–Kendall–Roberts (JKR) contact theory [60] is suitable for compliant materials with large short-range surface forces ($\mu > 1$). However, the determination of μ is not trivial for a film–substrate system, as E^* varies with δ and z_0 is difficult to determine. In one approach, DelRio *et al.* [15] used E^* at $F_N = 0$ and assumed that z_0 was equivalent to δ at $F_N = 0$. For $n = 18$ here, $E^* = 3.5$ GPa at $F_N = 0$ and $z_0 = 0.57$ nm, which results in $\mu = 0.34$. Thus,

even at moderate values of F_N, the DMT theory is a good approximation. As F_N increases, E^* increases, and μ decreases (due to substrate effects), pushing the system further into the DMT region. In another method, Grierson et al. [61] used the smallest reasonable values for E^* and z_0 to calculate an upper bound for μ; if the upper bound is less than unity, the DMT model is appropriate. For $n = 18$ here, the smallest reasonable values for E^* and z_0 are 1.4 GPa ($E_{film}/(1 - \nu_{film}^2)$) and 0.154 nm (the C–C bond distance), respectively, which results in an upper bound for μ of ≈ 2.3. With these extreme parameters, the value for μ indicates that the system is marginally in the JKR regime. However, even when the JKR model was used to extract w and E_{film} from the $F_N - \delta$ data in Fig. 2, the trends with n persisted, and the values increased by only $\approx 33\%$ and $\approx 7\%$, respectively. These variations represent the worst case scenario, as they assume purely JKR-like behavior. In reality, the system is better described with a self-consistent transition model, such as those developed by Maugis [62] using a simple Dugdale approximation and Greenwood and Johnson [63] based on the combination of two Hertzian pressure distributions, which would result in intermediate values for both w and E_{film}.

AFM lateral force measurements were used to determine F_F as a function of F_N for each film, which provided insight into the frictional properties in terms of chain length and deposition temperature. Overall, the short-chain monolayers exhibited larger F_F than the long-chain films. For $n = 5$ and 8, the monolayers are loosely packed and disordered, allowing for terminal gauche distortions (i.e., a 120° rotation along the C–C bond axis) to occur more easily [64]. Likewise, reductions in packing density facilitate molecular tilting and internal gauche distortions. Together, all three modes of deformation work to increase the friction, as observed by the increase in F_F with decreasing n in Fig. 3 and for alkanethiols on gold and alkylsilanes on mica [12], [21]. However, this trend does not hold for all n. In Fig. 3, F_F is smaller for $n = 12$ and 12e than for $n = 18$ and 18e, respectively, for all F_N. This deviation in behavior has been shown by others [25], [48] and explained by an increase in gauche defects at the terminal end and incomplete packing due to steric hindrance for $n = 18$; the latter effect is exacerbated and easily discernible with much longer chain monolayers, such as $n = 30$ [48]. Note than even small decreases in packing density can lead to an increase in the likelihood of viscoelastic deformation modes at the terminal end of the monolayer. Thus, it is possible for $n = 18$ films to be relatively more disordered at the surface and exhibit greater friction while simultaneously exhibiting a greater degree of order throughout the bulk of the film, as shown by the dichroic ratios in Table II.

Previous studies on the interfacial properties of SAMs have shown that the total friction force, F_F, arises from several interactions, as given by [26], [64]

$$F_F = F_I + F_D + \ldots = \tau A_I + \eta A_P + \ldots \quad (7)$$

where F_I is the interfacial friction, which is friction arising from adhesion normal to the contacting interface, F_D is the friction due to lateral deformation of the monolayer, and $\langle\ldots\rangle$
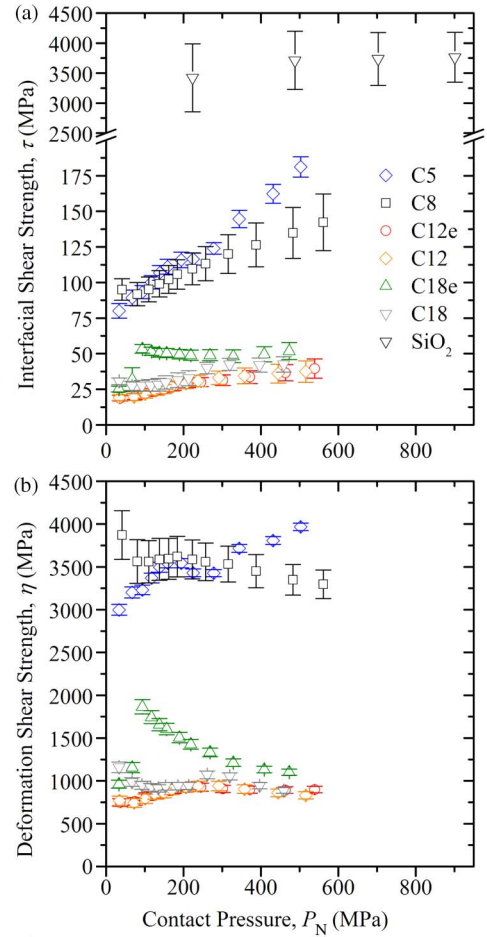

Fig. 4.   (a) Interfacial shear strength τ as a function of normal contact pressure P_N. (b) Deformation shear strength η as a function of normal contact pressure P_N. Error bars represent two standard deviations from the mean.

represents other potential sources, including electronic [65] and phononic [66] friction. F_D is traditionally used to describe both viscoelastic deformation and plastic plowing deformation. As there were no wear tracks observed during the lateral force measurements, F_D here is primarily taken to be due to viscoelastic dissipation. Given E_{film} for each n, (3) was used to find the interfacial contact area A_I and the projected sliding area A_P, which were then used with (7) to determine τ and η. The conversion of F_F to τ and η was not straightforward, however, because interfacial friction and deformation friction exist simultaneously. Consequently, each term was considered individually in an attempt to place upper bounds on both τ and η. That is, in the absence of deformation friction, what is the maximum τ exhibited by each monolayer, and in the absence of interfacial friction, what is the maximum η exhibited by each monolayer. The results for these upper bound estimates for τ and η are shown in Fig. 4(a) and (b), respectively, as a function of contact pressure $P_N = F_N/A_I$.

As shown in Fig. 4(a), the interfacial shear strength of the SiO$_2$ substrate was invariant with contact pressure ($\tau \approx 3500$ MPa), while τ for the alkylsilane monolayers exhibited a slight pressure dependence. $n = 5$ and 8 showed the largest τ values ($\tau \approx 80$ to 200 MPa) and a strong pressure dependence, whereas $n = 12e$, 12, 18e, and 18 were all very similar with
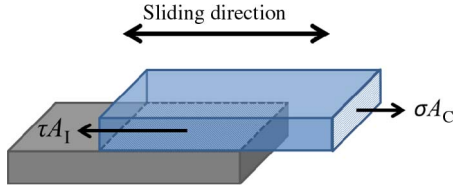
Fig. 5.   Schematic representation of two MEMS surfaces in sliding contact.

τ values ranging from 30 to 50 MPa and a relatively weak pressure dependence; the dependence on P_N is thought to arise from substantial deformation friction that occurs within the monolayer during sliding [67]. The interfacial shear strength for $n = 18e$ was greater than its condensed-phase counterpart, likely due to a decrease in packing density. However, τ values for $n = 12$ and 12e were equivalent within the experimental error. For all n, it was observed that the addition of an alkylsilane monolayer reduced the interfacial shear strength of the surface by as much as two orders of magnitude when compared with the SiO$_2$ substrate but that the relative reduction in τ was far greater than in F_F (see Fig. 3) because the alkylsilane monolayers exhibited elastic moduli much less than, and therefore contact radii much greater than, that of the underlying SiO$_2$ as determined by (3).

As shown in Fig. 4(b), the deformation shear strengths for $n = 5$ and 8 are on the order of 3000 to 4000 MPa, whereas $n = 12$ and 18 have η values between 800 and 1100 MPa. Larger η values for $n = 5$ and 8 can be explained using the same argument as mentioned earlier when comparing raw lateral forces; these films are relatively compliant and more disordered, which allows for gauche deformations, chain tilting, and increased interaction with the substrate. In addition, η was found to be relatively constant over this range of P_N for $n = 8$, 12, and 18. The stability in η for large n and the linear $F_F - F_N$ behavior as shown in Fig. 3 indicate that the lateral deformation in this P_N range is viscoelastic, not plastic, in nature. At larger P_N, superlinear $F_F - F_N$ behavior has been observed [21], [68] and attributed to nonlinear stiffening of the molecular chains under loading [26], [46]. In contrast, η for $n = 5$ increased dramatically with P_N, suggesting that this film is highly deformed during sliding by gross molecular plowing and possibly interactions with the underlying substrate.

A quantitative understanding of τ and η for SAMs and their underlying substrates is an important aspect of MEMS design, as many devices such as pop-up mirrors [69] and stepper motors [70] require not only contact but also sliding between surfaces. The flexibility provided to MEMS designers by the ability to control frictional interactions is illustrated by reference to Fig. 5, which is a schematic diagram of two MEMS components in sliding contact. A tensile stress, σ, acts over the cross section, area A_C, of the upper component leading to a frictional stress, τ, acting over the interfacial contact area, A_I, with the lower fixed component; under steady-state sliding conditions, $\sigma A_C = \tau A_I$ such that there is no net force on the upper component. The product σA_C can be regarded as an actuation force parallel to the interface for the sliding process and will have an upper bound set by the device power. If τ is large, as for unmodified surfaces, the upper bound on the actuation force places an upper

bound on A_I, and hence, designers must incorporate standoffs and bumpers to minimize A_I; the reduction of τ by surface modification removes such design constraints. Conversely, if τA_I is fixed by design and surface constraints, then a lower bound is set for σA_C. If A_C is also set by design constraints, this lower bound then imposes a lower bound on the fracture strength, σ_f, of the component, $\sigma_f > \sigma$. This strength constraint requires designers and manufacturers to optimize fabrication methods to minimize strength-controlling surface flaws [71], [72] and the chances of component failure [73]. If σ_f is set by fabrication methods, the lower bound of $\sigma_f A_C > \sigma A_C$ requires increases in the height of the upper component to increase A_C, thereby increasing the overall device size. The reduction of τ by surface modification clearly also removes the constraints on component strength and the related component size. Similar flexibility is provided by the ability to control adhesive interactions for actuation forces perpendicular to contacting interfaces; the reduction of w by surface modification removes fabrication and geometry constraints by removing the constraint on the lower bound of $\sigma_f h > w$, where h is the actuation distance required to separate the contact.

This work showed that alkylsilane SAMs of $n = 12e$ and 12 exhibit the smallest interfacial and deformation shear strength and therefore represent the optimal n of those studied for reducing friction at nominal loads and sliding velocities. However, it is important to note that $n = 18e$ and 18 were found to be more hydrophobic and exhibit smaller w. Therefore, care should be exercised to choose the alkylsilane chain length appropriate for the type of contact encountered when using these SAMs on MEMS devices. Ultimately, because alkylsilane SAMs are so effective at reducing the lateral friction force, MEMS designers can develop devices with smaller dimensions without additional processing steps to minimize A_I [74]–[76], thereby improving device sensitivity, power consumption, fabrication cost, and reliability.

V. SUMMARY AND CONCLUSION

In summary, the interfacial mechanical properties of alkylsilane SAMs on silicon were investigated by AFM normal force and lateral force measurements and correlated with molecular structure via NEXAFS spectroscopy. NEXAFS carbon K-edge spectra showed that R_I decreased from 0.40 to 0.12 as n decreased from 18 to 5, indicating that long-chain alkylsilanes are densely packed with near vertical chains but become more disordered or liquidlike as n decreases. Also, it was found that some monolayers of varying adsorption phase, such as $n = 18e$ and 18, show little difference in terms of relative order, whereas other monolayer films, such as $n = 12e$ and 12, show that liquid-expanded phase SAMs appear to be more disordered than their condensed-phase counterparts. Normal force spectroscopy demonstrated that E_{film} decreased from 1.2 to 0.67 GPa and w increased from 48.6 to 60.1 mJ · m^{-2} as n decreased from 18 to 5. Lateral force measurements showed that the adsorption of an alkylsilane monolayer reduces τ by as much as two orders of magnitude, from roughly 3500 MPa for bare SiO$_2$ to less than 50 MPa for $n = 12$ and 18, and that short-chain alkylsilanes (e.g., $n = 5$ and 8) exhibit an increased

pressure dependence on τ, a consequence of increased film disorder, smaller elastic moduli, and incomplete chain packing. However, because friction arises primarily from the deformation of the monolayer during sliding rather than through interfacial forces alone, η was also calculated and found to be on the order of 3500 MPa for $n = 5$ and 8 and 1000 MPa for SAMs of $n = 12$ and 18, respectively. In addition, η was pressure invariant for chain lengths greater than $n = 5$. Lastly, $n = 12$ was shown to be optimal for the chain lengths investigated here in terms of the ultimate reduction in lateral friction force. The development of similar structure–property relationships for different monolayer–substrate systems will eventually lead to the design and commercialization of reliable MEMS devices with contacting and sliding interfaces.

Acknowledgment

References

[1] H. C. Nathanson, W. E. Newell, R. A. Wickstrom, and J. R. Davis, Jr., "The resonant gate transistor," *IEEE Trans. Electron Devices*, vol. ED-14, no. 3, pp. 117–133, Mar. 1967.

[2] H. Guckel and D. W. Burns, "Planar processed polysilicon sealed cavities for pressure transducer arrays," in *Proc. IEDM*, 1984, vol. 30, pp. 223–225.

[3] W. C. Tang, T. H. Nguyen, M. W. Judy, and R. T. Howe, "Electrostatic comb drive of lateral polysilicon resonators," *Sens. Actuators A, Phys.*, vol. 21, no. 1–3, pp. 328–331, Feb. 1990.

[4] M. Madou, *Fundamentals of Microfabrication*. Boca Raton, FL: CRC Press, 1997.

[5] P. F. van Kessel, L. J. Hornbeck, R. E. Meier, and M. R. Douglass, "A MEMS-based projection display," *Proc. IEEE*, vol. 86, no. 8, pp. 1687–1704, Aug. 1998.

[6] R. Maboudian, "Surface processes in MEMS technology," *Surf. Sci. Rep.*, vol. 30, no. 6–8, pp. 207–268, Feb. 1998.

[7] A. D. Romig, Jr., M. T. Dugger, and P. J. McWhorter, "Materials issues in microelectro-mechanical devices: Science, engineering, manufacturability, and reliability," *Acta Mater.*, vol. 51, no. 19, pp. 5837–5866, Nov. 2003.

[8] S. L. Miller, M. S. Rodgers, G. LaVigne, J. J. Sniegowski, P. Clews, D. M. Tanner, and K. A. Peterson, "Failure modes in surface micromachined microelectromechanical actuators," in *Proc. IEEE Int. Annu. Reliab. Phys. Symp.*, Reno, NV, 1998, pp. 17–25.

[9] D. Tanner, N. F. Smith, D. J. Bowman, W. P. Eaton, and K. A. Peterson, "First reliability test of a surface micromachined microengine using SHiMMeR," in *Proc. SPIE*, 1997, vol. 3224, pp. 14–23.

[10] L. L. Mercado, S.-M. Kuo, T.-Y. T. Lee, and L. Liu, "Mechanics-based solution to RF MEMS switch stiction problem," *IEEE Trans. Compon. Packag. Technol.*, vol. 27, no. 3, pp. 560–567, Sep. 2004.

[11] A. Ulman, "Formation and structure of self-assembled monolayers," *Chem. Rev.*, vol. 96, no. 4, pp. 1533–1554, Jun. 1996.

[12] A. Lio, D. H. Charych, and M. Salmeron, "Comparative atomic force microscopy study of the chain length dependence of frictional properties of alkanethiols on gold and alkylsilanes on mica," *J. Phys. Chem. B*, vol. 101, no. 19, pp. 3800–3805, May 1997.

[13] J. E. Houston, C. M. Doelling, T. K. Vanderlick, Y. Hu, G. Scoles, I. Wenzl, and T. R. Lee, "Comparative study of the adhesion, friction, and

[14] mechanical properties of -CF3 and -CH3 terminated alkanethiol monolayers," *Langmuir*, vol. 21, no. 9, pp. 3926–3932, Apr. 2005.

[14] G. Oncins, C. Vericat, and F. Sanz, "Mechanical properties of alkanethiol monolayers studied by force spectroscopy," *J. Chem. Phys.*, vol. 128, no. 4, p. 044701, Jan. 2008.

[15] F. W. DelRio, K. L. Steffens, C. Jaye, D. A. Fischer, and R. F. Cook, "Elastic, adhesive, and charge transport properties of a metal-molecule-metal junction: The role of molecular orientation, order, and coverage," *Langmuir*, vol. 26, no. 3, pp. 1688–1699, Feb. 2010.

[16] D. Alamarguy, O. Schneegans, S. Noel, and L. Boyer, "Correlation between the electrical and mechanical behaviors of a nanocontact with an alkanethiol monolayer," *Appl. Surf. Sci.*, vol. 225, no. 1–4, pp. 309–317, Mar. 2004.

[17] U. Srinivasan, J. D. Foster, U. Habib, R. T. Howe, R. Maboudian, D. C. Senft, and M. T. Dugger, "Lubrication of polysilicon micromechanisms with self-assembled monolayers," in *Proc. Solid-State Sens. Actuators Workshop*, Hilton Head Island, SC, 1998, pp. 156–161.

[18] W. R. Ashurst, C. Yau, C. Carraro, C. Lee, R. T. Howe, and R. Maboudian, "Alkene based monolayer films as anti-stiction coatings for polysilicon MEMS," *Sens. Actuators A, Phys.*, vol. 91, no. 3, pp. 239–248, Jul. 2001.

[19] D. S. Grierson, A. R. Konicek, G. E. Wabiszewski, A. V. Sumant, M. P. DeBoer, A. D. Corwin, and R. W. Carpick, "Characterization of microscale wear in a polysilicon-based MEMS device using AFM and PEEM-NEXAFS spectromicroscopy," *Tribol. Lett.*, vol. 36, no. 3, pp. 233–238, Dec. 2009.

[20] X. Xiao, G. Liu, D. H. Charych, and M. Salmeron, "Preparation, structure, and mechanical stability of alkylsilane monolayers on mica," *Langmuir*, vol. 11, no. 5, pp. 1600–1604, May 1995.

[21] X. Xiao, J. Hu, D. H. Charych, and M. Salmeron, "Chain length dependence of the frictional properties of alkylsilane molecules self-assembled on mica studied by atomic force microscopy," *Langmuir*, vol. 12, no. 2, pp. 235–237, Jan. 1996.

[22] F. Tian, X. Xiao, M. M. T. Loy, C. Wang, and C. Bai, "Humidity and temperature effect on frictional properties of mica and alkylsilane monolayer self-assembled on mica," *Langmuir*, vol. 15, no. 1, pp. 244–249, Jan. 1999.

[23] V. V. Tsukruk and V. Bliznyuk, "Adhesive and friction forces between chemically modified silicon and silicon nitride surfaces," *Langmuir*, vol. 14, no. 2, pp. 446–455, Jan. 1998.

[24] L. Qian, F. Tian, and X. Xiao, "Tribological properties of self-assembled monolayers and their substrates under various humid environments," *Tribol. Lett.*, vol. 15, no. 3, pp. 169–176, Oct. 2003.

[25] D. H. Lee, T. Oh, and K. Cho, "Combined effect of chain length and phase state on adhesion/friction behavior of self-assembled monolayers," *J. Phys. Chem. B*, vol. 109, no. 22, pp. 11 301–11 306, Jun. 2005.

[26] E. E. Flater, W. R. Ashurst, and R. W. Carpick, "Nanotribology of octadecyltrichlorosilane monolayers and silicon: Self-mated versus unmated interfaces and local packing density effects," *Langmuir*, vol. 23, no. 18, pp. 9242–9252, Aug. 2007.

[27] M. J. Brukman, G. O. Marco, T. D. Dunbar, L. D. Boardman, and R. W. Carpick, "Nanotribological properties of alkanephosphonic acid self-assembled monolayers on aluminum oxide: Effects of fluorination and substrate crystallinity," *Langmuir*, vol. 22, no. 9, pp. 3988–3998, Apr. 2006.

[28] H. Yoshizawa, Y. L. Chen, and J. Israelachvili, "Fundamental mechanisms of interfacial friction. 1. Relation between adhesion and friction," *J. Phys. Chem.*, vol. 97, no. 16, pp. 4128–4140, Apr. 1993.

[29] B. V. Derjaguin, V. M. Muller, and Y. P. Toporov, "Effect of contact deformations on the adhesion of particles," *J. Colloid Interface Sci.*, vol. 53, no. 2, pp. 314–326, Nov. 1975.

[30] V. M. Muller, V. S. Yushchenko, and B. V. Derjaguin, "General theoretical consideration of the influence of surface forces on contact deformations and the reciprocal adhesion of elastic spherical particles," *J. Colloid Interface Sci.*, vol. 92, no. 1, pp. 92–101, Mar. 1983.

[31] F. W. DelRio, C. Jaye, D. A. Fischer, and R. F. Cook, "Elastic and adhesive properties of alkanethiol self-assembled monolayers on gold," *Appl. Phys. Lett.*, vol. 94, no. 13, p. 131 909, Mar. 2009.

[32] Q. Li, K. S. Kim, and A. Rydberg, "Lateral force calibration of an atomic force microscope with a diamagnetic levitation spring system," *Rev. Sci. Instrum.*, vol. 77, no. 6, p. 065105, Jun. 2006.

[33] J. B. Brzoska, I. B. Azouz, and F. Rondelez, "Silanization of solid substrates: A step toward reproducibility," *Langmuir*, vol. 10, no. 11, pp. 4367–4373, Nov. 1994.

[34] J. D. LeGrange and J. L. Markham, "Effects of surface hydration on the deposition of silane monolayers on silica," *Langmuir*, vol. 9, no. 7, pp. 1749–1753, Jul. 1993.

[35] C. Carraro, O. W. Yauw, M. M. Sung, and R. Maboudian, "Observation of three growth mechanisms in self-assembled monolayers," *J. Phys. Chem. B*, vol. 102, no. 23, pp. 4441–4445, Jun. 1998.

[36] J. L. Hutter and J. Bechhoefer, "Calibration of atomic force microscope tips," *Rev. Sci. Instrum.*, vol. 64, no. 7, pp. 1868–1873, Jul. 1993.

[37] L. S. Dongmo, J. S. Villarubia, S. N. Jones, T. B. Renegar, M. T. Postek, and J. F. Song, "Experimental test of blind tip reconstruction for scanning probe microscopy," *Ultramicroscopy*, vol. 85, no. 3, pp. 141–153, Nov. 2000.

[38] B. D. Booth, S. G. Vilt, C. McCabe, and G. K. Jennings, "Tribology of monolayer films: Comparison between n-alkanethiols on gold and n-alkyl trichlorosilanes on silicon," *Langmuir*, vol. 25, no. 17, pp. 9995–10 001, Sep. 2009.

[39] M. J. Stevens, "Thoughts on the structure of alkylsilane monolayers," *Langmuir*, vol. 15, no. 8, pp. 2773–2778, Apr. 1999.

[40] B. G. Bush, F. W. Del Rio, J. Opatkiewicz, R. Maboudian, and C. Carraro, "Effect of formation temperature and roughness on surface potential of octadecyl-trichlorosilane self-assembled monolayer on silicon surfaces," *J. Phys. Chem. A*, vol. 111, no. 49, pp. 12 339–12 343, Dec. 2007.

[41] J. Stöhr, *NEXAFS Spectroscopy*. Berlin, Germany: Springer-Verlag, 1992.

[42] K. Beirbaum, M. Kinzler, C. Wöll, and M. Grunze, "A near edge X-ray absorption fine structure spectroscopy and X-ray photoelectron spectroscopy study of the film properties of self-assembled monolayers of organosilanes on oxidized Si(100)," *Langmuir*, vol. 11, no. 2, pp. 512–518, Feb. 1995.

[43] D. A. Outka, J. Stöhr, J. P. Rabe, and J. D. Swalen, "The orientation of Langmuir–Blodgett monolayers using NEXAFS," *J. Chem. Phys.*, vol. 88, no. 6, pp. 4076–4087, Mar. 1988.

[44] H. Xu and G. M. Pharr, "An improved relation for the effective elastic compliance of a film/substrate system during indentation by a flat cylindrical punch," *Scr. Mater.*, vol. 55, no. 4, pp. 315–318, Aug. 2006.

[45] J. Dolbow and M. Gosz, "Effect of out-of-plane properties of a polyimide film on the stress fields in microelectronic structures," *Mech. Mater.*, vol. 23, no. 4, pp. 311–321, Aug. 1996.

[46] M. Wang, K. M. Liechti, V. Srinivasan, J. M. White, P. J. Rossky, and M. T. Stone, "A hybrid continuum-molecular analysis of interfacial force microscope experiments on a self-assembled monolayer," *J. Appl. Mech.*, vol. 73, no. 5, pp. 769–777, Sep. 2006.

[47] H. Hoffman, U. Mayer, and A. Krischanitz, "Structure of aklysiloxane monolayers on silicon surfaces investigated by external reflection infrared spectroscopy," *Langmuir*, vol. 11, no. 4, pp. 1304–1312, Apr. 1995.

[48] S. Sambasivan, S. Hsieh, D. A. Fischer, and S. M. Hsu, "Effect of self-assembled monolayer film order on nanofriction," *J. Vac. Sci. Technol. A, Vac. Surf. Films*, vol. 24, no. 4, pp. 1484–1488, Jul. 2006.

[49] J. Genzer, K. Efimenko, and D. A. Fischer, "Molecular orientation and grafting density in semifluorinated self-assembled monolayers on mono-, di-, and trichloro silanes on silica substrates," *Langmuir*, vol. 18, no. 24, pp. 9307–9311, Nov. 2002.

[50] H. W. Fox and W. A. Zisman, "The spreading of liquid on low-energy surfaces. III. Hydrocarbon surfaces," *J. Colloid Sci.*, vol. 7, no. 4, pp. 428–442, Aug. 1952.

[51] J. Israelachvili, *Intermolecular and Surface Forces*. Boston, MA: Academic, 1992.

[52] R. C. Thomas, J. E. Houston, R. M. Crooks, T. Kim, and T. A. Michalske, "Probing adhesion forces at the molecular scale," *J. Amer. Chem. Soc.*, vol. 117, no. 13, pp. 3830–3834, Apr. 1995.

[53] C. E. H. Berger, K. O. van der Werf, R. P. H. Kooyman, B. G. de Grooth, and J. Greve, "Functional group imaging by adhesion AFM applied to lipid monolayers," *Langmuir*, vol. 11, no. 11, pp. 4188–4192, Nov. 1995.

[54] H. J. Butt, K. Graf, and M. Kappl, *Physics and Chemistry of Interfaces*. Weinheim, Germany: Wiley-VCH, 2003.

[55] R. G. Nuzzo, B. R. Zegarski, and L. H. Dubois, "Fundamental studies of the chemisorption of organosulfur compounds on gold (111). Implications for molecular self-assembly on gold surfaces," *J. Amer. Chem. Soc.*, vol. 109, no. 3, pp. 733–740, Feb. 1987.

[56] W. D. Callister, *Materials Science and Engineering: An Introduction*. New York: Wiley, 2000.

[57] F. W. Del Rio, D. M. Rampulla, C. Jaye, G. Stan, R. S. Gates, D. A. Fischer, and R. F. Cook, "Structure–property relationships for methyl-terminated alkyl self-assembled monolayers," *Chem. Phys. Lett.*, vol. 512, no. 4–6, pp. 243–246, Aug. 2011.

[58] V. B. Engelkes and C. D. Frisbie, "Simultaneous nanoindentation and electron tunneling through alkanethiol self-assembled monolayers," *J. Phys. Chem. B*, vol. 110, no. 20, pp. 10 011–10 020, May 2006.

[59] D. Tabor, "Surface forces and surface interactions," *J. Colloid Interface Sci.*, vol. 58, no. 1, pp. 2–13, Jan. 1977.

[60] K. L. Johnson, K. Kendall, and A. D. Roberts, "Surface energy and the contact of elastic solids," *Proc. R. Soc. Lond. A, Math. Phys. Sci.*, vol. 324, no. 1558, pp. 301–313, Sep. 1971.

[61] D. S. Grierson, E. E. Flater, and R. W. Carpick, "Accounting for the JKR-DMT transition in adhesion and friction measurements with atomic force microscopy," *J. Adhes. Sci. Technol.*, vol. 19, no. 3–5, pp. 291–311, Mar. 2005.

[62] D. Maugis, "Adhesion of spheres: The JKR-DMT transition using a Dugdale model," *J. Colloid Interface Sci.*, vol. 150, no. 1, pp. 243–269, Apr. 1992.

[63] J. A. Greenwood and K. L. Johnson, "An alternative to the Maugis model of adhesion between elastic spheres," *J. Phys. D, Appl. Phys.*, vol. 31, no. 22, pp. 3279–3290, Nov. 1998.

[64] M. Salmeron, "Generation of defects in model lubricant monolayers and their contribution to energy dissipation in friction," *Tribol. Lett.*, vol. 10, no. 1/2, pp. 69–79, Jan. 2001.

[65] B. N. J. Persson and A. I. Volokitin, "Electronic friction of physisorbed molecules," *J. Chem. Phys.*, vol. 103, no. 19, pp. 8679–8683, Nov. 1995.

[66] M. S. Tomassone, J. B. Sokoloff, A. Widom, and J. Krim, "Dominance of phonon friction for a xenon film on a silver (111) surface," *Phys. Rev. Lett.*, vol. 79, no. 24, pp. 4798–4801, Dec. 1997.

[67] O. Piétrement and M. Troyon, "Study of the interfacial shear strength pressure dependence by modulated lateral force microscopy," *Langmuir*, vol. 17, no. 21, pp. 6540–6546, Oct. 2001.

[68] L. Qian and X. Xiao, "Tip in situ chemical modification and its effects on tribological measurements," *Langmuir*, vol. 16, no. 2, pp. 662–670, Jan. 2000.

[69] J. J. Sniegowski and E. J. Garcia, "Microfabricated actuators and their application to optics," in *Proc. SPIE Miniaturized Syst. Micro-Opt. Micromech.*, 1995, pp. 46–64. [Online]. Available: http://mems.sandia.gov/tech-info/doc/microfaboptics.pdf

[70] R. Yeh, S. Hollar, and K. S. J. Pister, "Single mask, large force, and large displacement electrostatic linear inchworm motors," *J. Microelectromech. Syst.*, vol. 11, no. 4, pp. 330–336, Aug. 2002.

[71] M. S. Gaither, F. W. DelRio, R. S. Gates, E. R. Fuller, Jr., and R. F. Cook, "Strength distribution of single-crystal silicon theta-like specimens," *Scr. Mater.*, vol. 63, no. 4, pp. 422–425, Aug. 2010.

[72] M. S. Gaither, F. W. DelRio, R. S. Gates, and R. F. Cook, "Deformation and fracture of single-crystal silicon theta-like specimens," *J. Mater. Res.*, vol. 26, no. 20, pp. 2575–2589, Oct. 2011.

[73] E. E. Flater, A. D. Corwin, M. P. deBoer, and R. W. Carpick, "In situ wear studies of surface micromachined interfaces subject to controlled loading," *Wear*, vol. 260, no. 6, pp. 580–593, Mar. 2006.

[74] L. S. Fan, Y. C. Tai, and R. S. Muller, "Integrated movable micromechanical structures for sensors and actuators," *IEEE Trans. Electron Devices*, vol. 35, no. 6, pp. 724–730, Jun. 1988.

[75] Y. Yee, K. Chun, and J. D. Lee, "Polysilicon surface modification technique to reduce sticking of microstructures," in *Proc. 8th Int. Conf. Solid-State Sens. Actuators*, Stockholm, Sweden, Jun. 1995, pp. 206–209.

[76] M. R. Houston, R. T. Howe, and R. Maboudian, "Effect of hydrogen termination on the work of adhesion between polycrystalline silicon surfaces," *J. Appl. Phys.*, vol. 81, no. 8, pp. 3474–3483, Apr. 1997.

Brian G. Bush, photograph and biography not available at the time of publication.

Frank W. Del Rio, photograph and biography not available at the time of publication.

Cherno Jaye, photograph and biography not available at the time of publication.

Daniel A. Fischer, photograph and biography not available at the time of publication.

Robert F. Cook, photograph and biography not available at the time of publication.